Journal of Fluids and Structures 61 (2016) 249–261

Contents lists available at ScienceDirect

Journal of Fluids and Structures

journal homepage: www.elsevier.com/locate/jfs

Impact of ground and wheel boundary conditions on numerical simulation of the high-speed train aerodynamic performance

Jie Zhang [a,1], Jing-juan Li [a,1], Hong-qi Tian [a], Guang-jun Gao [a,*], John Sheridan [b]

[a] Key Laboratory of Traffic Safety on Track of Ministry of Education, School of Traffic & Transportation Engineering, Central South University, Changsha 410075, China

[b] Department of Mechanical and Aerospace Engineering, Monash University, Clayton, Victoria 3800, Australia

ARTICLE INFO

Article history:
Received 29 July 2014
Accepted 22 October 2015
Available online 29 December 2015

Keywords:
Moving ground condition
Rotating wheel
Aerodynamic performance
High-speed train

ABSTRACT

In this paper, the aerodynamic performance of a high speed train with moving ground and rotating wheels (MG&RW) conditions has been investigated using Computational Fluid Dynamic (CFD). The numerical simulations under the condition of stationary ground and moving ground are also compared and discussed. To validate the accuracy of the mesh resolution and methodology, the CFD results are compared with the wind tunnel test results. The aerodynamic forces, unsteady and time average flow fields around the high-speed train are analyzed. The main aim of this study is to investigate how the moving ground and wheel conditions influence the numerical simulation results. The moving ground condition eliminates the effects of boundary layers of ground and rail track, which results in the velocity under the train being faster than in the stationary ground condition. As a result, the drag of every bogie and the pressure on the bottom surface calculated under moving ground conditions is found to be higher than that under the stationary ground condition. The wheel rotation boundary condition has little effect on the force distribution on the bottom surface of the train. However, at the bogie regions, it increases the velocity of airflow around and behind the wheel, causing a change of the pressure distribution and an increment of the wheels' drag. Consequently, the total drag of the train in moving ground with rotating wheel condition is nearly equal to that of condition with the moving ground considered. In addition, the total drag of bogies just takes up 10.4% in all in the stationary ground condition, and it accounts for 12.7% in the moving ground condition and 15.1% in the moving ground with rotating wheel condition.

1. Introduction

With the rapid development of high-speed trains around the world, the investigation of three-dimensional flow around them has become of significant importance in the rail industry. The execution of proper aerodynamic design requires an extensive understanding of the relevant flow phenomena and aerodynamic performance. In recent years, there has been

* Corresponding author.
E-mail address: gjgao@csu.edu.cn (G.-j. Gao).
[1] These two authors contributed equally to this work.

http://dx.doi.org/10.1016/j.jfluidstructs.2015.10.006
0889-9746/

considerable work done that studies high-speed trains' aerodynamic performance. The basic tools used include full-scale tests, wind tunnel tests and computational fluid dynamics (CFD) (Xiao et al., 2013).

When the train runs, the movement of the train will include wheel rotation and the relative motion between the wind and the train, as well as the relative motion between the stationary ground and the moving train. Full-scale tests are undoubtedly the most reliable approach because they investigate on the real operation of the train. However, in the case of train aerodynamics, full-scale tests and wind tunnel tests are difficult (Baker, 2010). Full-scale measurements strongly depend on environment and very often a large number of runs have to be carried out to obtain the reliable results.

With regard to wind tunnel tests for the investigation of train aerodynamic performances, the velocity inlet condition is given to simulate the relative motion between the train and the wind. The wind tunnel tests are difficult because of the ground effect. In terms of the aerodynamic force measurement, the ground effect simulation will affect the results, and is difficult to be eliminated. Although some new technologies, such as installation of the moving ground and suction-from-below devices on the floor under the train have been found effective to reduce or eliminate the ground effect (Xiao et al., 2013; Baker, 1991, 2010; Kwon et al., 2001), the application of these technologies is limited due to their high cost and complex operation. Most wind tunnel tests have not considered the moving ground and rotating wheel conditions, as demonstrated in published papers (Orellano and Schober, 2006; Schober et al., 2010; Huang et al., 2013; Huang et al.,2012; Bell et al, 2014). In addition, the measurement and display of the flow field in wind tunnel tests require special techniques capable of qualitative and quantitative analysis.

CFD is widely used since it is capable of efficiently computing and visualizing the flow field around trains. Lots of research about the aerodynamic performance using CFD has been done previously (Miao and Gao, 2012; Krajnovic et al., 2012; Hemida and Krajnovic, 2010; Raghunathana et al., 2002; Diedrichs, 2008). Zheng and Yang, (2011) have investigated the aerodynamic performance of high-speed trains in open air using Detached-Eddy Simulations (DES). Yao et al. (2013) have researched the mechanism of vortex formation and evolution in the train flow field using DES. A large number of studies have been undertaken and reported in Zhang et al. (2011), Zhang and Xiong (2011) and He (2011). In these numerical simulations, the ground movement relative to the train is considered by giving the ground the same velocity as the inlet flow, but the wheel-rotation condition is usually ignored. According to some CFD results in numerical simulations of a high-speed train with bogies (Zhang and Xiong, 2011; Yao et al, 2012), we discovered that the total drag of the head car is bigger than the tail car, but the results are found to be contradictory to this in wind tunnel tests. In the research of this paper, we have previously found discrepancies between wind tunnel and CFD results of simulation under stationary ground condition that suggest the total drag of the head car could in fact be lower than the tail car.

Based on the discussion above, the details of aerodynamic performance have not been analyzed for the running train. And the difference of aerodynamic performance of trains tested under stationary ground condition and moving ground with wheels rotating condition has not been researched. The aim of this paper is to investigate the aerodynamic performance of trains in the moving ground and rotating-wheel conditions using CFD tools, and study how the moving ground and wheel conditions influence the numerical simulation results. The mechanism effect of the moving ground and wheel condition based on the numerical simulation results is analyzed. The numerical simulation of the wind tunnel test with stationary ground and with moving ground are investigated as case 1 and case 2. In case 3, the numerical simulation is performed under the moving ground with rotating wheel (MG&RW) condition to investigate the aerodynamic performance of the train and the impact of the wheel rotation condition on the results.

This paper is organized as follows. In Section 2, the geometry, the numerical method, meshes and boundary conditions are given together with the cases studied. The train aerodynamic forces in case 1 are then compared with the wind tunnel test results to validate the accuracy of the resolution of the mesh and methodology. In Section 3, the drag in each case is compared and analyzed. The mechanism of the moving ground and rotating wheel conditions and how they affect the numerical simulation results are then explained. Finally, conclusions are drawn in Section 4.

2. CFD analysis

2.1. Computational model and boundary conditions

The wind tunnel model and the numerical models are basically the same, being a simplified version of the CRH2 train, which contains bogies, wheels and windshields, as shown in Fig. 1. It is grouped as three cars (the head car, the middle car and the tail car). The model scale is 1/8th, so the total length of the train is $L=9.5516$ m and its projected cross section area is $A=0.175$ m^2. Moreover, to make accurate and independent force measurements for each car and to guarantee that the flow field of the train is not influenced, the internal and external windshields between adjacent cars were separated by nested form in wind tunnel tests (Huang et al., 2012), as illustrated in Fig. 1. To reduce any influence of the gaps on the computational results, the gaps between adjacent cars were retained in the computational model.

The CFD results are compared with the results from wind tunnel tests. The measurements were made in the second test section of 8 m $\times$ 6 m wind tunnel in China Aerodynamics Research and Development Center (CARDC). The test setup is shown in Fig. 2(a). To reduce the thickness of the approaching boundary layer, a fixed ground board with a rotating table device was installed especially for the high-speed train tests. The distance of the floor device to the lower wall of the wind tunnel is 1.06 m. Then the test section is transformed into the one for high-speed train tests, which is 4.94 m high and

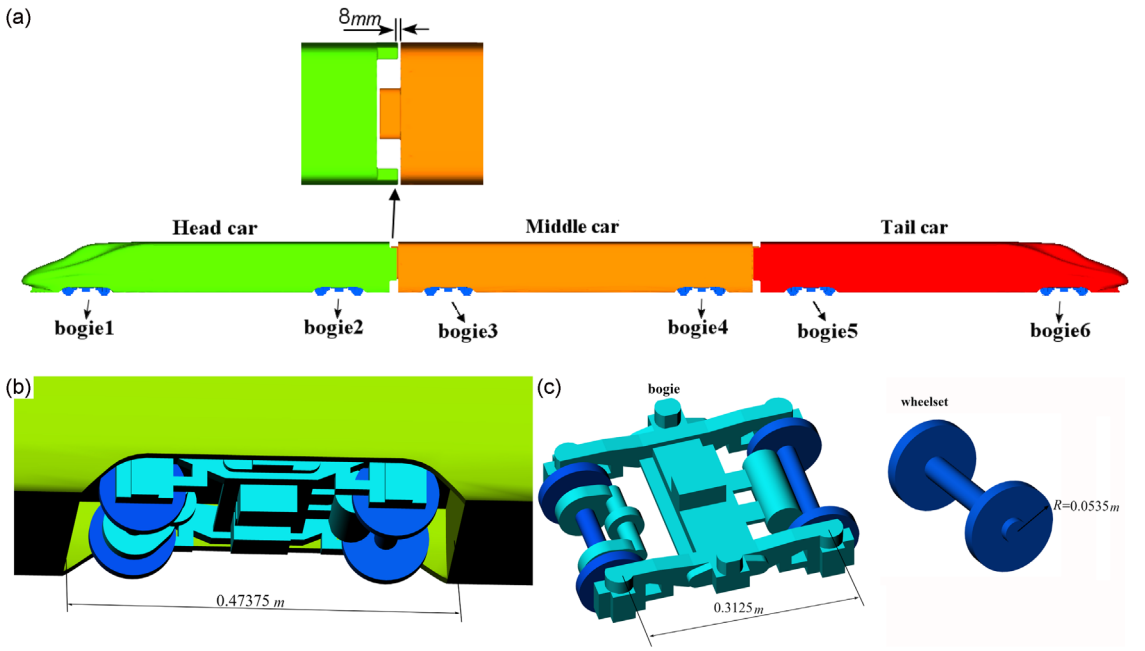

Fig. 1. CRH2 train model: (a) Train model, (b) Installation region of the bogie, (c) Bogie and wheel models.

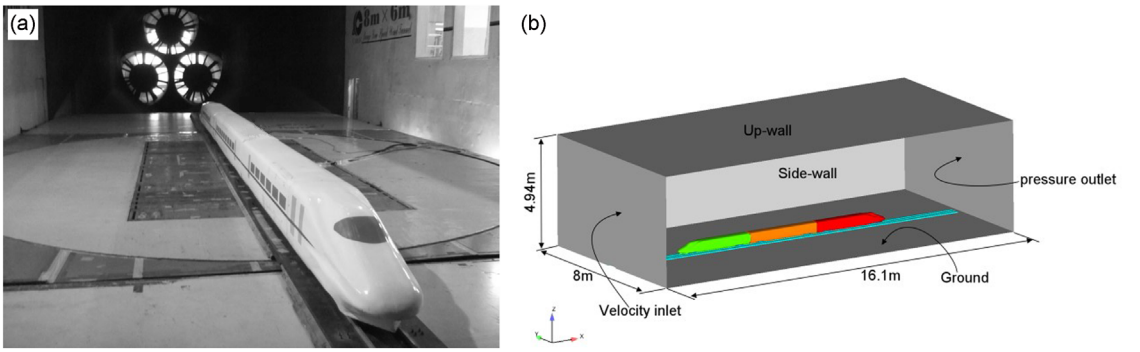

Fig. 2. (a) Experimental setup. Taken from Zhang and Zhou, 2013, (b) Wind tunnel geometry for CFD.

16.1 m long (Zhang and Zhou, 2013). The practical cross-section area is 39.5 m^2. The computational domain is set up based on the wind tunnel test field as shown in Fig. 2(b). The space dimensions and velocities are denoted by x and $U_{upstream}$ in the stream wise direction, y in the span-wise direction and z in the vertical direction. The cross-section area of computational domain is 39.5 m^2. This gives a small blockage ratio of 0.443%.

In each case of the numerical simulations investigated, the flow enters the computational domain with a uniform velocity profile that is constant in time. The velocity inlet is given with uniform wind speed of 60 m/s. Its corresponding Reynolds number is the same as that of the wind tunnel test, which is equal to 1.85×10^6 based on the free-stream velocity and the height of the train. The pressure outlet is given a static pressure of zero. The top and side surfaces of the domain are set as no-slip walls. The train surface is also treated as no-slip wall boundary. Other boundary condition details for each numerical simulation in this paper are summarized in Table 1. In case 3, the angular velocity of the rotating wheels and the speed of the moving ground are set according to the train speed.

2.2. Grid generation for CFD simulation

The OpenFOAM mesh generator package was applied to build the hexahedral dominated mesh around the train, as shown in Fig. 3. There is a fine structure around the body, which allows for grid refinement in the wall-normal direction near the body boundaries. The size of the finest train surface mesh is 2.8 mm. And there is a refinement box of 12000 mm × 1000 mm × 625 mm around the train with the maximum mesh size of 11.2 mm. To catch the boundary layer from the wall surface, 10 prism layers in a boundary are applied from the train surface, completing the 3D volume mesh. The

Table 1
Boundary condition details for CFD analysis.

Case	Surface	Boundary condition	Detail
Case 1: stationary ground condition	Ground	Wall	Stationary
Case 2: moving ground condition	Ground	Moving wall	60 m/s
Case 3: moving ground and rotating wheel (MG&RW) condition	Ground	Moving wall	60 m/s
	Wheels	Moving wall	1121.4953 rad/s

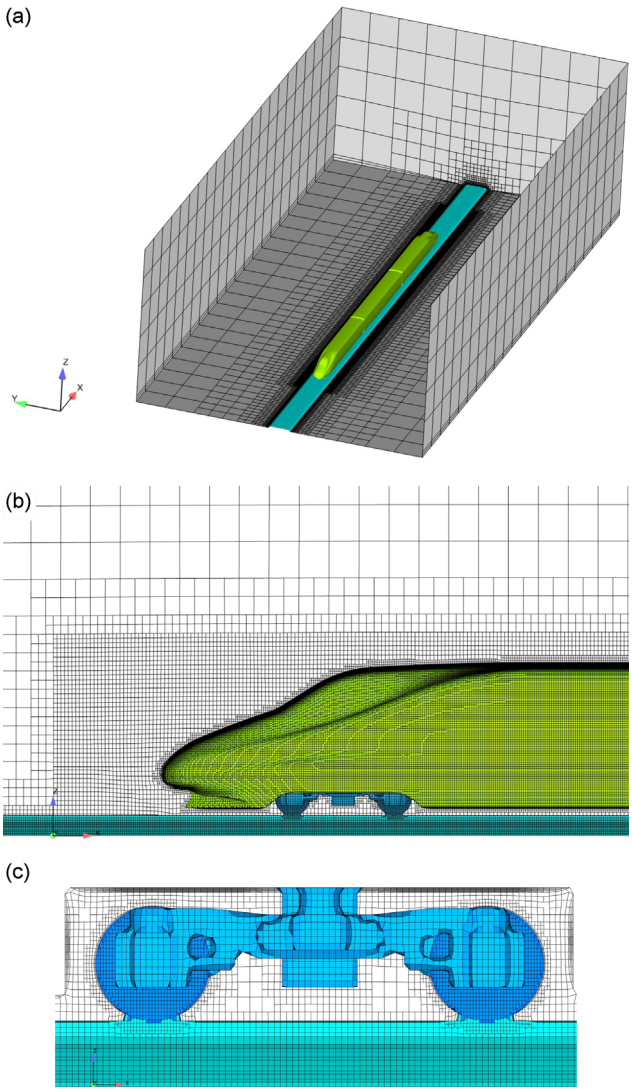

Fig. 3. Computational mesh around the train: (a) Global view of the mesh, (b) Mesh distribution around the train, (c) Mesh distribution around the wheel.

thickness of the first boundary layer is 0.42 mm to ensure the use of wall function in k-epsilon turbulence model (FLUENT User's Guide, 2011). There are approximately 16 150 000 volume meshes. The boundary layers and the volume mesh configuration are shown in Fig. 3(b).

2.3. Methodology for CFD analysis

In this study, the commercial CFD solver ANSYS FLUENT was used. Based on Reynolds averaged motion equation, the turbulence model theory provides a group of turbulence averaged closed equations, arrived at from a combination of theory and experience (FLUENT User's Guide, 2011). The numerical simulation in this paper used the Detached Eddy Simulation (DES) approach (Spalart et al., 1997; Spalart, 2009; Nasif et al., 2014). In the DES turbulence model, an unsteady RANS model

is used in the near wall regions and Large Eddy Simulation in the region where large turbulence scales play a dominant role. A realizable k–ε model is chosen in the vicinity of walls because it is known to provide superior performance for flows involving rotation, boundary layers with adverse pressure gradients, separation and recirculation (Kang et al., 2012; Guilmineau et al., 2011). In the simulations of this paper, the Finite Volume Method (FVM) based on cell centers was adopted for the discretization of the governing equations. Simulations were performed using a pressure-based solver. The SIMPLE (Semi-Implicit Method for Pressure-Linked Equations) algorithm was used in the computational method to couple the pressure and the velocity fields. A bounded central differencing scheme (FLUENT User's Guide, 2011) was chosen for solving the momentum equation. A second-order upwind (FLUENT User's Guide, 2011) scheme was chosen for solving the k and ε equations.

Time discretization method uses the unsteady calculating method of dual-time step format. The dual-time step method uses two kinds of time, which are virtual time and physical time, to introduce something which is similar to virtual time iteration process in Newton iteration at the freezing real-time point and this inner iteration process would improve lost accuracy. The LU-SGS (Lower-upper symmetric gauss–seidel) implicit scheme (Jameson and Yoon, 1987; FLUENT User's Guide, 2011) is used for time integral.

2.4. Post-processing

2.4.1. Drag coefficients

The aerodynamic drag of a train consists of the pressure drag and the viscous drag. In this paper the drag we discussed is the sum of pressure drag and viscous drag as default (Tian, 2007). The component of the aerodynamic drag projected to the train axis is in the stream-wise direction. The non-dimensional drag coefficient and the non-dimensional pressure coefficient can be defined as:

$$C_d = \frac{F}{0.5\rho U_{upstream}^2 A}, \tag{2.1}$$

$$C_p = \frac{P - P_0}{0.5\rho U_{upstream}^2}, \tag{2.2}$$

where, F is the drag force that contains the viscous force and the pressure-difference force. C_d is the drag force coefficient. C_p is the pressure coefficient. ρ is the density of air which is 1.225 kg/m^3. A is the projected cross-section area of the train, which is 0.175 m^2 herein. P_0 is the reference pressure is 0. P is the static pressure on the train surface.

2.4.2. Time-averaged flow fields and quantities

The flow around a train is turbulent, as shown in Fig. 7. The drag coefficients of the train change over time. For every case, the non-dimensional time "$tU_{\mathrm{upstream}}/A^{1/2}$" from 0 to 50 is not considered in calculating the averaged quantities, since these time-steps correspond to a transient period when the flow becomes unsteady, as demonstrated in Fig. 4. However, as time increases the solution values become relatively steady. The drag forces and other quantities are then calculated by taking the average value over the non-dimensional time from 50 to 160.

2.4.3. Vortex visualization technique

The iso-surface of constant Q is used to describe the transient vortex structure. An iso-surface with positive Q isolates the areas where the strength of the rotation overcomes the strain, thus meaning these iso-surfaces can be considered in defining vortex envelopes (Hemida et al., 2005). The flow computed in this paper is regarded as incompressible flow at a low speed. The value of Q is given by

$$Q = -\frac{1}{2}u_{i,j}u_{j,i},$$

where $u_{i,j}$ *and* $u_{j,i}$ are the velocity gradient tensors. A region of positive Q implies that there is a vortex (Hemida et al., 2005).

2.5. Results and validation

The train aerodynamic forces under the condition of stationary ground are compared with the results taken from Zhang and Zhou (2013). Therefore, if the drag coefficients C_d calculated are similar to the results in wind tunnel tests, the CFD analysis can be considered valid. As shown in Table 2 the maximum error of the simulation calculation is less than 2%, which means the resolution of the mesh and methodology is sufficient to achieve accurate numerical results.

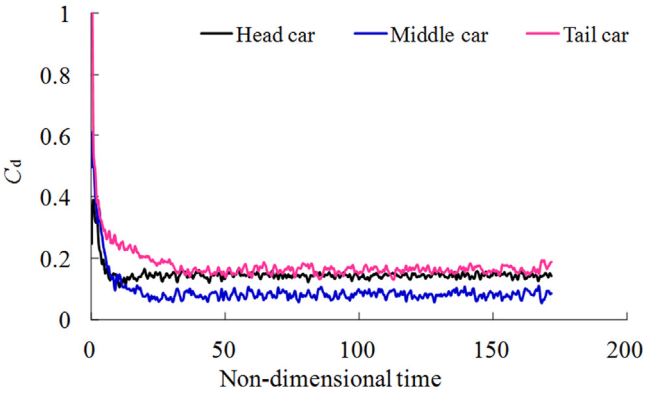

Fig. 4. Time history curves of C_d of each car.

Table 2
Numerical results vs. wind tunnel test results.

Method	C_d	
	Head car	Tail car
Wind tunnel test (Zhang and Zhou, 2013)	0.145	0.163
Numerical simulation	0.144	0.160

Table 3
Results of the numerical simulation.

Component	C_d		
	Case 1: stationary ground condition	Case 2: moving ground condition	Case 3: MG&RW condition
Head car (without bogies)	0.120	0.113	0.111
Bogie 1	0.020	0.023	0.024
Bogie 2	0.004	0.006	0.008
Total head car	0.144	0.142	0.143
Middle car (without bogies)	0.074	0.086	0.082
Bogie 3	0.004	0.006	0.009
Bogie 4	0.003	0.006	0.008
Total middle car	0.081	0.098	0.099
Tail car (without bogies)	0.151	0.157	0.156
Bogie 5	0.003	0.004	0.005
Bogie 6	0.006	0.007	0.008
Total tail car	0.160	0.168	0.169
Total	0.385	0.408	0.411

3. Results and discussion

3.1. Force analyses

The time-averaged drag coefficients obtained from the three simulation cases are demonstrated in Table 3. The total drag of the train is the lowest in the stationary ground situation. For case 3, with both the moving ground and rotating wheels considered, its total drag is nearly equal to that of case 2 which is just taken into the moving ground considered. Compared with the total drag of the train in case 1, the drag in case 2 increase by 6.0% and in case 3 by 6.8%, which means that the moving ground and rotating wheel conditions have a certain effect on the aerodynamic drag of the high-speed train. The drag of each bogie increases in the moving ground condition and in the MG&RW case it increases significantly. Under each condition, the total drag of the head car is lower than that of the tail car. And the drag difference between the head car and tail car increases in case 2 and case 3. The difference is 11.1% under the stationary ground condition, while it is 18.3% under the moving ground condition, and 18.2% under the MG&RW condition.

It can be seen in Table 3 that the drag of the middle car (without bogies) and tail car (without bogies) in case 2 and case 3 are higher than that in case 1, while the head car's drag is lower. Compared with drag of each car in case 1 (the stationary ground condition), the drag of the head car body (i.e. without bogies) decreases by 5.8% in case 2 (the moving ground

condition) and 7.5% in case 3 (the MG&RW condition). For the middle car body and the tail car body the reduction percentage is 16.2% and 4.0% in case 2, 10.8% and 3.3% in case 3. The drag of each bogie in case 3 is the largest, as presented in Table 3. The ratio of the total drag of bogies to the total drag of the train is 10.4% in case 1, and this becomes 12.7% in case 2 and 15.1% in case 3. The drag decrease of the head car with the increment of the middle and tail cars' drag leads to a bigger drag difference between the head car and tail car in case 2 and case 3. As a result, the moving ground boundary condition and rotating wheel boundary condition have an effect on the ratios of the drag of every component of the train to the total drag, this is especially the case for the bogies. The impact of this mechanism will be analysed in detail in next section.

3.2. Impact of ground and wheel boundary condition on the flow field of the train

3.2.1. Mechanism of the ground effect

High-speed trains are thin, long bodies that run close to the ground. In both wind tunnel test and numerical simulation the velocity inlet condition is set to simulate the relative motion between the train and the wind. Under the stationary ground condition, the train will be affected by the ground effect due to the boundary layer of the airflow. Fig. 5 shows the boundary layer of flow which is 1 m away from the side of the train in the stationary ground condition and moving ground condition. With the stationary ground condition there is a boundary layer on the ground. And the streamwise velocity changes uniformly as one moves away from the wall. The thickness of boundary layer increases along the train. It lowers the velocity of the flow under the train especially the bogie areas of the middle car and tail car. Under the moving ground condition, this boundary layer disappears.

When the inlet wind run into the train, flow around the train becomes unsteady and turbulent. Then the boundary layer of the ground near the train is broken. But the ground effect persists, and as a result, the velocity of bottom of the train becomes slower in the stationary condition than that under the moving ground condition. The phenomenon is shown and discussed in later section. Meanwhile, this makes the drag value of each bogie calculated in the stationary ground condition smaller than that under the moving ground condition.

Viscous drag is a part of the aerodynamic drag. It is primarily determined by the boundary layer thickness near the walls of the train. The boundary layers give rise to the skewing of the streamline around the train. In Fig. 6(b), the middle section of each car is chosen to show the boundary layer thickness around the train by the velocity contour with a value of 59.7 m/s (99.5% of the inflow velocity (EnSight User's Guide, 2013)). It can be seen that the boundary thickness near the train body of each car in the three cases are basically the same. The boundary layer thickness in the middle section of the head car is smaller than that of other sections. The moving ground condition only alters the flow field under the train.

3.2.2. Effect of the ground and wheel conditions

To identify the effect of the ground and wheel boundary conditions on the flow field around the train, the instantaneous vortex structure of the train at the same non-dimensional time 170 in each case is depicted in Fig. 7. The time-averaged pressure contour distribution is demonstrated in Fig. 8. The moving ground and rotating wheel conditions do not change the instantaneous upper flow structures of the train. In Fig. 7(a) the instantaneous flow structures around the train in case 1 is shown. There are a few vortices around the upper part of the head car, while many vortices are turned up around the middle car and tail car. The more vortices are, the more turbulent the flow is. Then the upper flow of the middle car and tail car are more turbulent than that of the head car. The flow separation occurs most often on the tail car between the skirt and nose. However, the instantaneous flow structures in the wake are different from case 2 and case 3 to case 1, seeing Fig. 7(b) and Fig. 7(c). Influenced by the ground effect, the wake flow velocity is lower in case 1 compared with case 2 and case 3, as discussed in Section 3.2.1. Then the wake vortices progress downstream and remain close to the ground in case 1. In case 3 and case 2, two separated dominant tail vortices of the main instantaneous flow structure are more obvious as Fig. 7 (b) shown. And they progress downstream and are lifted off the ground in Fig. 7(c).

As the vortices progress downstream, the area behind the train where vortex is produced frequently will present with positive pressure. It can be seen in Fig. 8 that the time-averaged pressure distributions on the upper surface of the train and

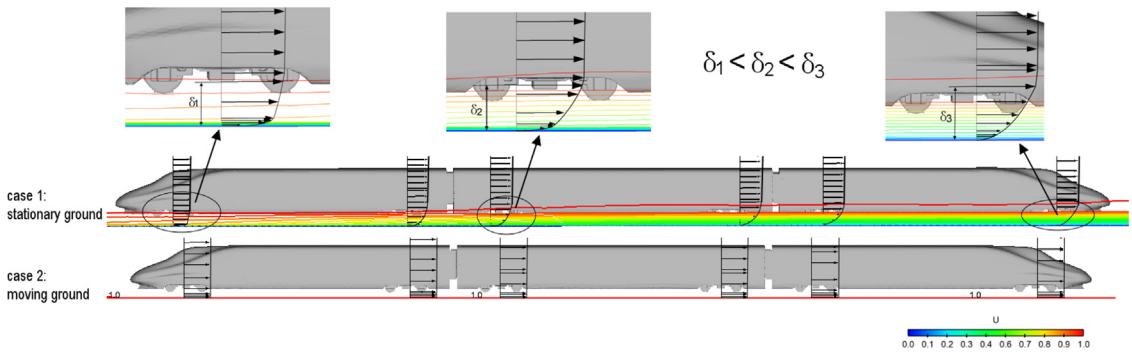

Fig. 5. Boundary layer of flow in the plane 1 m away from the side of the train.

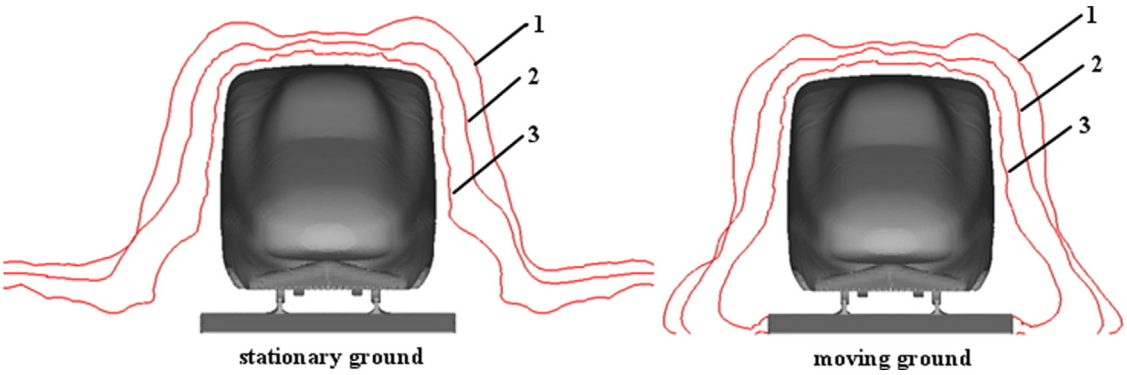

Fig. 6. Boundary layer around the train: 1 Boundary layer thickness in the middle section of the tail car, 2 Boundary layer thickness in the middle section of the middle car, 3 Boundary layer thickness in the middle section of the head car.

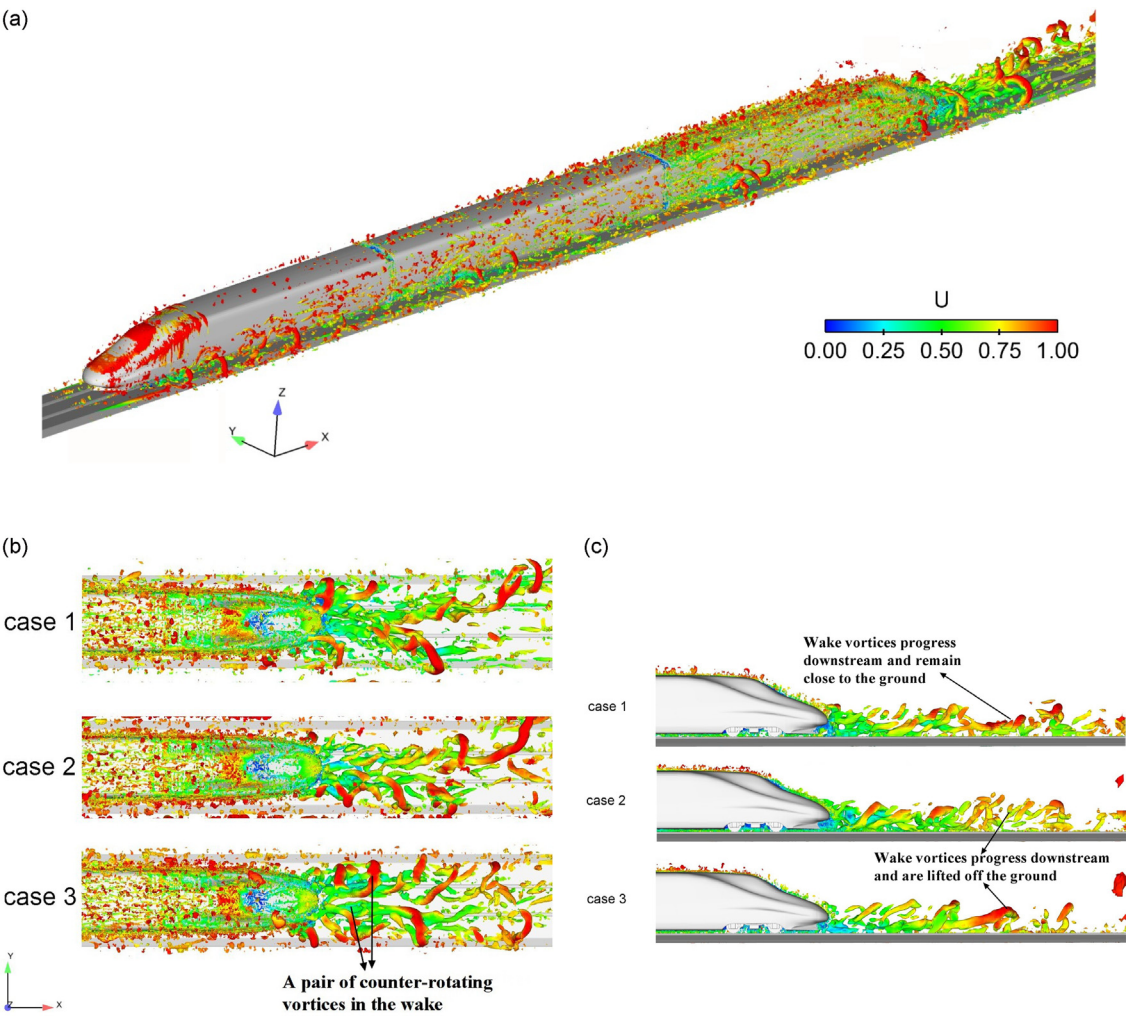

Fig. 7. Instantaneous iso-surface plot of *Q*-criteria, coloured by non-dimensional velocity *U* (*Q*=50000): (a) Instantanenous vortex structure around the train in case 1, (b) Wake vortex structure, (c) Half wake vortex.

around the head car and middle car calculated in each case do not differ greatly. However, the time-averaged positive pressure area in the wake increases in case 2 and case 3 compared with case 1.

To further analyze this, the pressure distribution on the centerline of the train is shown in Fig. 9(a) and (b) to investigate the impact of rotating wheel and ground boundary conditions on the drag of the train. Fig. 9(a) shows the pressure

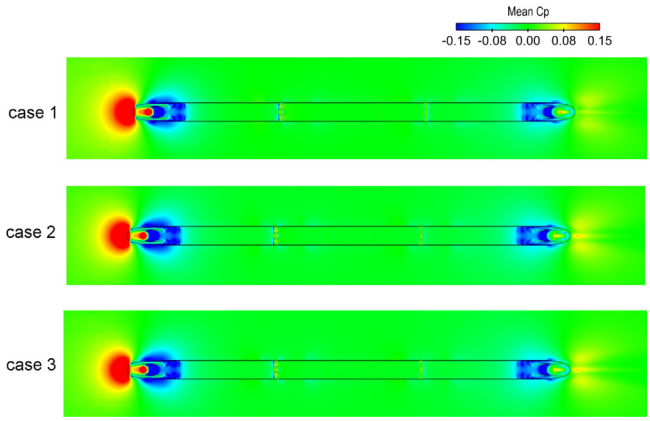

Fig. 8. Mean static pressure contour on the train surface and the horizontal plane located at z/h=0.054.

distribution of the upper centerline of the train. It is found that the pressure distributions of the upper flow of each case are very similar. The largest pressure is found on the head car nose, which faces the flow stream.

In Table 3, the drag of the middle car (without bogies) and tail car (without bogies) in case 2 and case 3 is bigger than that in case 1. It can be found why this has happened from the peressure on the bottom of the train, because the different pressure between the front equipment cabin cover and back equipment cabin cover in the *x* direction contributes to the drag of the car body, as shown in Fig. 9(b) and Fig. 9(c). Except for the bogie installation region of bogie 1, that the negative pressures of the bogie installation region are lower and the positive pressures are higher in case 2 and case 3, compared with case 1. The pressure distributions on the bottom surfaces in bogie installation regions in case 2 and case 3 are almost the same, seeing Fig. 9(c), which are different from that in case 1. Since the pressure distribution characteristics at bogie 2 and bogie 5 regions are similar to these at bogie 4 and bogie 3 regions, respectively, the surface pressure at bogie 2 and bogie 5 regions will be not presented in Fig. 9(c). In each bogie area the maximum positive pressure is mainly distributed at the end of the bogie installation region, where there is blockage by the underbody from the equipment cabin cover. And on the surface of the eqiupment cabin cover behind the rear wheel of bogies, there are two symmetry positive areas in case 2 and case 3, but it is not obvious in case 1 except for the bogie installation region of bogie 1 and bogie 4. Due to the ground effects discussed in Section 3.2.1, the flow under the train is faster in case 2 and case 3, resulting in a lower bottom flow pressure and a higher positive pressure on the equipment cabin cover behind the bogie where the flow is blocked. The pressure distribution under the MG&RW condition does not change significantly compared with that under the moving ground without rotating wheels. This proves that the wheel rotation boundary condition has little effect on the force distribution on the bottom surface of the train.

In Table 3, it shows that the drag of each bogie in case 2 and case 3 is bigger than in case 1. To find out the reason for this, further resarch has been done. The mean static pressure field of bogies in each case is showed in Fig. 10(a). The mean pressure coefficient distributions on the wheelsets of bogie 3 in each case are shown in Fig. 10(b). And the corresponding pressure coefficient curves along the centerline of wheels in the right side are demonstrated in Fig. 10(c) and Fig. 10(d), respectively. In Fig. 10(a) it can be seen that the positive pressure area on the bottom surface of bogies in case 2 and case 3 is larger than that in case 1. For each bogie in each case, the pressure of the rear wheelset is relatively higher than that of the front wheelset. Because there is a flow being deflected from the equipment cabin cover, which causes the flow velocity around the rear wheelset is lower. Fig. 10(b) shows that the pressure on the side surfaces of wheels in case 3 is lower than that in other two cases. The largest negative pressure area is found in case 3 on the side surface of every wheel, while the least is in case 1. In Fig. 10(c) the negetive pressure of the wheel in case 3 is lower than in other cases. Then the pressure difference on the wheel is the largest in case 3, which leads to the highest drag of wheels. Consquently, the drag of each bogie is the largest as showed in Table 3. For the stationary ground boundary condition, the boundary layer of the ground affects the flow velocity between the ballast and the bottom of the train. Additionally, it decreases the calculation accuracy of the pressure of wheels.

To investigate the reason for difference pressure distributions on the wheel surfaces, the time-averaged velocity field was studied. Since the velocity field distribution characteristics of bogie 2 and bogie 5 regions are similar to these of bogie 4 and bogie 3 regions, respectively, we just select four bogie regions to quickly view the velocity field around the wheels in Fig. 11. Because of the slender shape, small aspect ratio and limited space between the train and the ballast, the flow velocity under the train decreases along the train length direction. The velocity of the flow into the region of bogie 1 is the highest in all bogie regions of the train. The high speed flow causing large surface area of bogie 1 has a negative pressure, seeing Fig. 10(a). In Fig. 11 the velocity in V1, V2, V3 and V4 areas in case 1 are different from these in case 2 and case 3. The velocity are higher and the area are larger in case 2 and case 3. Due to the ground effect, the velocity speed of the airflow into the bogie regions in case 1 is lower than that in case 2 and case 3. As a result, the positive pressure of the wheel tread surface in the windward side is larger in case 3 and case 2 as shown in Fig. 10. Furthermore, it can be observed that the flow structure around the wheels do change in the wheel rotating case. The airflow behind the wheel rises and moves rapidly with the

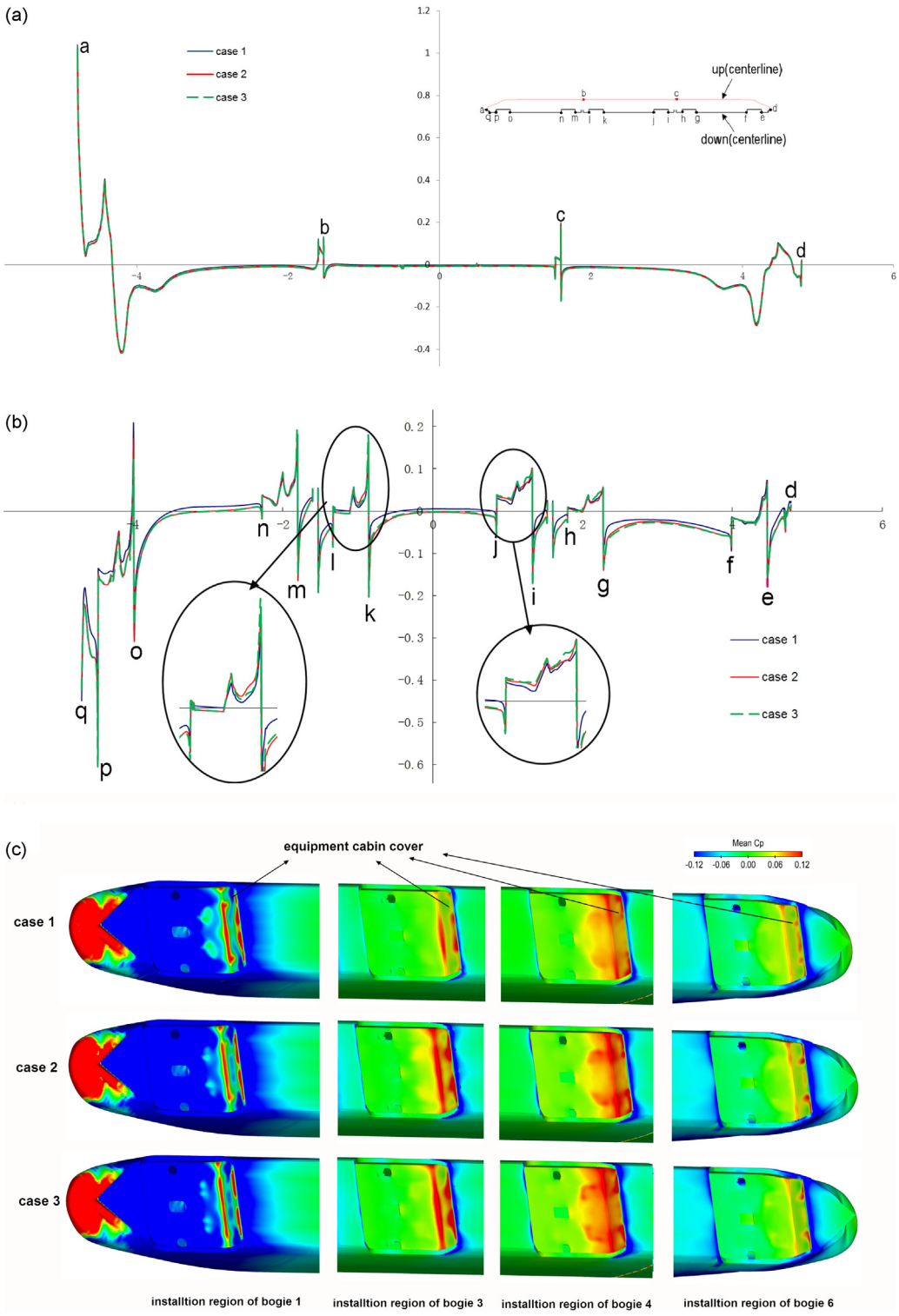

Fig. 9. Pressure distribution on the train: (a) Pressure distribution along upper centerline of the train, (b) Pressure distribution along bottom centerline of the train, (c) Pressure field on the bottom surface of bogie regions.

wheel rotating, which leads to flowing upward and forward. The velocity structures, such as V5, V6, V7, V8, V9, V10, V11 and V12, disappear in case 3, but some other low speed velocity areas turn up, seeing V13, V14 and V15. The rotating wheel condition plays a siginficant role in understanding the flow characteristics around the wheels.

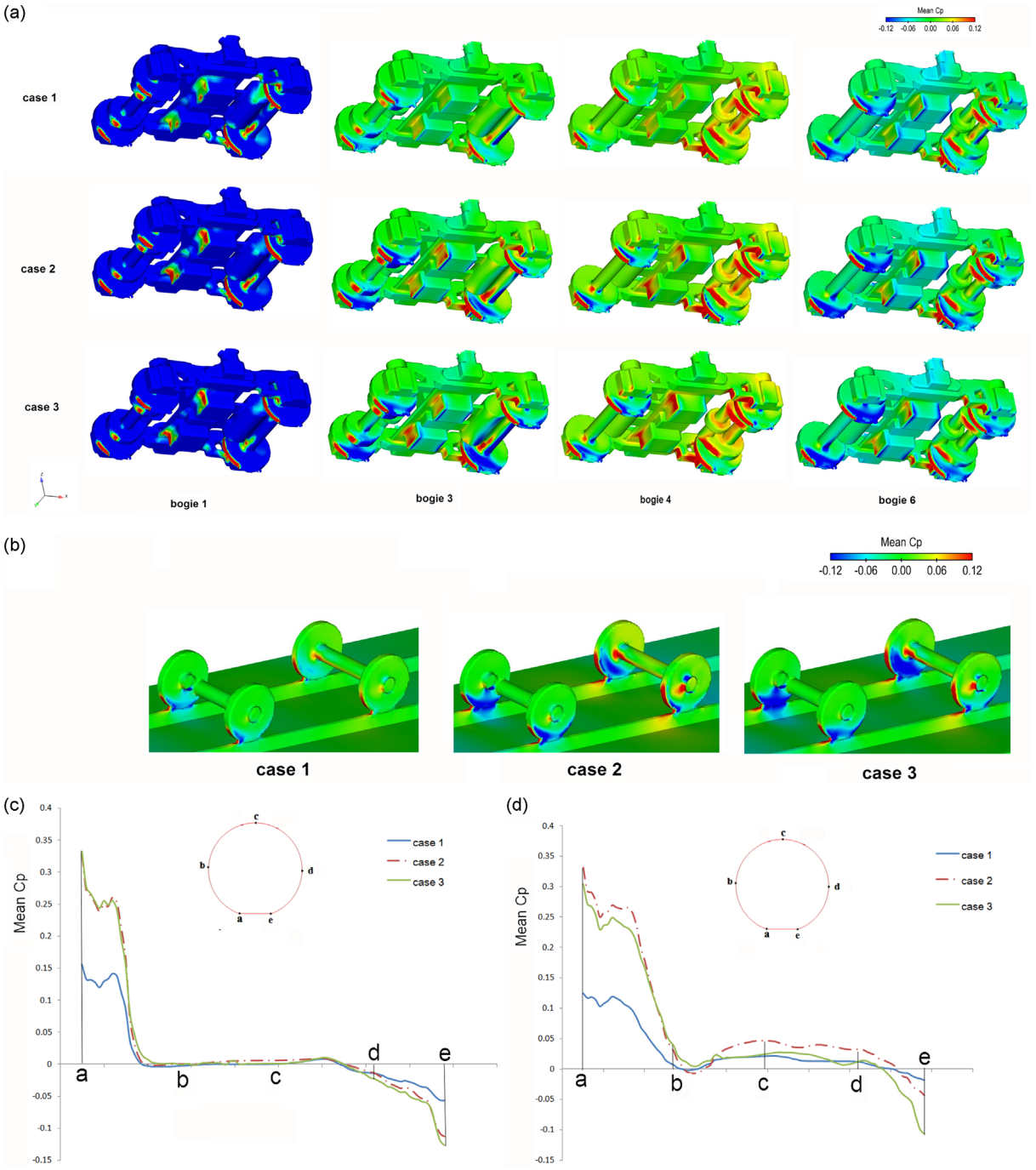

Fig. 10. Pressure distributions on bogies: (a) Mean static pressure on the bottom surfaces of bogies, (b) Mean static pressure on the wheel surfaces, (c) Mean static pressure distribution along the centerline of the front wheel of bogie 3, (d) Mean static pressure distribution along the centerline of the rear wheel of bogie 3.

4. Conclusions

In this study, the aerodynamic performances of a high-speed train under stationary ground, moving ground and MG&RW conditions were investigated using CFD. Based on the results, the following conclusions can be drawn:

(1) Under the moving ground and MG&RW conditions, the total drag of the train is higher than under the stationary ground situation. When the moving ground and rotating wheels are considered together, the total drag is nearly equal to that

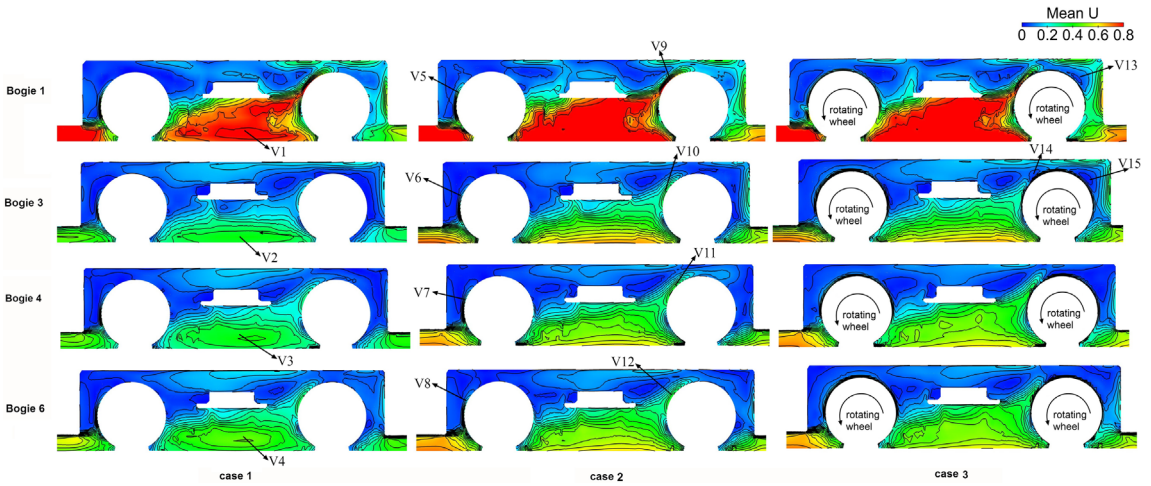

Fig. 11. Time-averaged velocity contour on the center longitudinal plane of wheels for bogies 1, 3, 4 and 6.

only under the moving ground considered. The drag of each bogie increases in the moving ground condition and in the MG&RW case it increases significantly. The ratio of the total drag of bogies to the total drag of the train is 10.4% in the stationary ground condition, and this becomes 12.7% in the moving ground condition and 15.1% in the moving ground with rotating wheel condition.

(2) The mechanism of drag increased for the MG&RW condition can be explained as follows. The moving ground condition eliminates the impact of the boundary layers of ground and rail track, which results in the velocity of bottom of the train being faster than that under the stationary ground condition. This also causes the drag value of every bogie and the drag of the tail and middle cars calculated under the moving ground condition to be higher than that under the stationary ground condition. The rotating wheel boundary condition with moving ground has little effect on the force distribution on the bottom surface of the train. However, in the bogie regions, the rotating wheel condition increases the velocity around and behind the wheel, causing a change of the pressure distribution and an increment of the wheels' drag.

(3) The numerical simulation results show that the flow fields around the wheels in the MG&RW condition are quite different from that under the stationary ground condition and moving ground condition. The stationary ground boundary condition decreases the calculation accuracy of the pressure of wheels. Thus, it is necessary to use the MG&RW condition in numerical simulations of the high-speed train aerodynamic performance to accurately simulate the detailed flow phenomenon in wheel regions of the train.

Acknowledgements

The authors acknowledge the computing resources provided by the Institute of High-speed Train of Central South University, China.

This work was accomplished by the supports of the National Natural Science Foundation of China (Grant Nos. U1334205, U1134203 and 51075401), the Program for New Century Excellent Talents in University of China (Grant No. NCET-10-083), the Hunan Provincial Innovation Foundation for Postgraduate of China (Grant No. CX2014B061).

References

Baker, C.J., 1991. Wind tunnel tests to obtain train aerodynamic drag coefficients: reynolds number and ground simulation effects[J]. Journal of Wind Engineering and Industrial Aerodynamics 38 (1), 23–28.

Baker, C., 2010. The flow around high speed trains. Journal of Wind Engineering and Industrial Aerodynamics 98 (6–7), 277–298.

Bell, J.R., Burton, D., Thompson, M., Herbst, A., Sheridan, J., 2014. Wind tunnel analysis of the slipstream and wake of a high-speed train[J]. Journal of Wind Engineering and Industrial Aerodynamics 134, 122–138.

EnSight User's Guide, Computational Engineering International, 2013.

B. Diedrichs, Aerodynamic calculations of crosswind stability of a high-speed train using control volumes of arbitrary polyhedral shape. BBAA VI International Colloquium on: Bluff Bodies Aerodynamic and Applications. Milano, Italy, 20–24 July.

Fluent Inc. FLUENT User's Guide. 2011.

He, Dehua, 2011. Research of aerodynamic simulation on 350km/h high-speed EMU. China Academy of Railway. Science. In Chinese.

Guilmineau, Emmanuel, Deng, GanBo, Wackers, Jeroen, 2011. Numerical simulation with a DES approach for automotive flows. Journal of Fluids and Structures 27 (5–6), 807–816.

Hemida Hassan, Krajnovic Sinisa, Davidson Lars, 2005. Large-Eddy Simulation of the flow around a simplified high speed train under the influence of a cross-wind. 17th AIAA Computational Fluid Dynamics Conference, 6-9 June, Toronto, Ontario Canada.

Hemida, H., Krajnovic, S., 2010. LES study of the influence of the nose shape and yaw angles on flow structures around trains. Journal of Wind Engineering and Industrial Aerodynamics 98 (1), 34–46.

Huang, Zhi-xiang, Chen, Li, Zhang, Weizhuo, 2013. Study on simulation manner of wind tunnel test of high-speed train model. Journal of Railway Science and Engineering 10 (3), 87–93. In Chinese.
Huang, Zhi-xiang, Chen, Li, Jiang, Ke-Lin, 2012. Wind tunnel test of air-drag reduction schemes of high-speed trains. Journal of The China Railway Society 34 (4), 16–21. In Chinese.
Jameson, A., Yoon, S., 1987. Lower-upper implicit schemes with multiple grids for the Euler equations. AIAA Journal 25 (7), 929–935.
Krajnovic, S., Ringqvist, P., Nakade, K., Basara, B., 2012. Large eddy simulation of the flow around a simplified train moving through a crosswind flow. Journal of Wind Engineering and Industrial Aerodynamics 110, 86–99.
Kang, S.O., Jun, S.O., Park, H.I., Song, K.S., Kee, J.D., Kim, K.H., Lee, D.H., 2012. Actively translating a rear diffuser device for the aerodynamic drag reduction of a passenger car. International Journal of Automotive Technology 13 (4), 583–592.
Kwon, H.B., Park, Y.W., Lee, D.H., Kim, M.S., 2001. Wind tunnel experiments on Korean high-speed trains using various ground simulation techniques. Journal of Wind Engineering and Industrial Aerodynamics 89, 1179–1195.
Miao, Xiu-juan, Guang-jun, Gao, 2012. Aerodynamic performance of train under cross-wind based on DES. Journal of Central South University (Science and Technology) 7 (43), 2855–2860. In Chinese.
Nasif, G., Barron, R.M., Balachandar, R., 2014. DES evaluation of near-wake characteristics in a shallow flow. Journal of Fluids and Structures 45, 153–163.
A. Orellano, M. Schober, Aerodynamic performance of a typical high-speed train, in: Proceedings of the 4th WSEAS International Conference on Fluid Mechanics and Aerodynamics, Elounda, Greece, August 21–23, 2006, pp.18–25.
Raghunathana, R.S., Kim, H.D., Setoguchic, T., 2002. Aerodynamics of high-speed railway train. Progress in Aerospace Sciences 38 (6–7), 469–514.
Schober, M., Weise, M., Orellano, A., Deeg, P., Wetzel, W., 2010. Wind tunnel investigation of an ICE 3 end car on three standard ground scenarios. Journal of Wind Engineering and Industrial Aerodynamics 98 (6/7), 345–352.
P.R. Spalart, W.H. Jou, M. Strelets, S.R. Allmaras, Comments on the feas1ibility of LES for wings, and on a hybrid RANS/LES approach[C]. In: Proceedings of first AFOSR international conference on DNS/LES, Ruston, Louisiana. Greyden Press, 4–8 Aug, 1997.
Spalart, P.R., 2009. Detached-eddy simulation. Annual Review of Fluid Mechanics 41, 181–202.
Tian, Hong-qi, 2007. Train aerodynamics. China Railway Press, Beijing.
Xiao, Jingping, Huang, Zhixiang, Chen, Li, 2013. Review of aerodynamic investigations for High Speed train. Mechanics in Engineering 35(2), 1–12. in Chinese.
Yao, S.B., Guo, D.L., Yang, G.W., Li, M.G., 2012. Distribution of high-speed train aerodynamic drag. Journal of the China Railway Society 34 (7), 18–23. in Chinese.
Yao, Shuan-bao, Sun, Zhen-Xu, Guo, Dilong, Chen, Da-wei, Yang, Guo-wei, 2013. Numerical study on wake characteristics of high-speed trains. Acta Mechanica Sinica 29 (6), 811–822.
Zhang, Jie, Liang, Xifeng, Liu, Tanghong, Lu, Linfeng, 2011. Optimization Research on aerodynamic shape of passenger car body with strong crosswind. Journal of Central South University: Science and Technology 42 (11), 3578–3584. In Chinese.
Zhang, Miao, Xiong, Hongbing, 2011. Effects of different components on the aerodynamics of high-speed train. Manufacturing Automation (4), 202–204+217. In Chinese.
Zhang, Zaizhong, Zhou, Dan, 2013. Wind tunnel experiment on aerodynamic characteristic of streamline head of high speed train with different head of high speed train with different head shapes. Journal of Central South University: Science and Technology 44 (06), 2603–2608. in Chinese.
H. Zheng, G. Yang, Investigation of aerodynamic performance of high-speed train by detached eddy simulation. 1st International Workshop on High-Speed and Intercity Railways, IWHIR 2011, July 19–22, 2011, Shenzhen, Hong Kong, China.